Localization of sterols and oxysterols in mouse brain reveals distinct spatial cholesterol metabolism

Eylan Yutuc[a] , Roberto Angelini[a] , Mark Baumert[b], Natalia Mast[c] , Irina Pikuleva[c] , Jillian Newton[d], Malcolm R. Clench[d] , David O. F. Skibinski[a] , Owain W. Howell[a] , Yuqin Wang[a,1] , and William J. Griffiths[a,1]

[a]Institute of Life Science, Swansea University Medical School, SA2 8PP Swansea, Wales, United Kingdom; [b]Advion Limited, Harlow, Essex CM20 2NQ, United Kingdom; [c]Department of Ophthalmology and Visual Sciences, Case Western Reserve University, Cleveland, OH 44106; and [d]Centre for Mass Spectrometry Imaging, Biomolecular Research Centre, Sheffield Hallam University, S1 1WB Sheffield, United Kingdom

Dysregulated cholesterol metabolism is implicated in a number of neurological disorders. Many sterols, including cholesterol and its precursors and metabolites, are biologically active and important for proper brain function. However, spatial cholesterol metabolism in brain and the resulting sterol distributions are poorly defined. To better understand cholesterol metabolism in situ across the complex functional regions of brain, we have developed on-tissue enzyme-assisted derivatization in combination with microliquid extraction for surface analysis and liquid chromatography-mass spectrometry to locate sterols in tissue slices (10 µm) of mouse brain. The method provides sterolomic analysis at 400-µm spot diameter with a limit of quantification of 0.01 ng/mm². It overcomes the limitations of previous mass spectrometry imaging techniques in analysis of low-abundance and difficult-to-ionize sterol molecules, allowing isomer differentiation and structure identification. Here we demonstrate the spatial distribution and quantification of multiple sterols involved in cholesterol metabolic pathways in wild-type and *cholesterol 24S-hydroxylase* knockout mouse brain. The technology described provides a powerful tool for future studies of spatial cholesterol metabolism in healthy and diseased tissues.

liquid chromatography-mass spectrometry | brain | cholesterol | 24S-hydroxycholesterol | 24S,25-epoxycholesterol

The brain is a remarkably complex organ in terms of anatomy and function. Little is known about the landscape of the metabolome or lipidome across the brain. The brain represents a major repository of unesterified cholesterol in mammals; almost 25% of total body cholesterol is found in brain and the central nervous system (CNS), where it is present at a level of about 20 µg/mg (wet weight) (1). As cholesterol cannot cross the blood brain barrier (BBB) and be imported from the periphery, essentially all cholesterol in brain is biosynthesized in brain. Inborn errors of cholesterol biosynthesis often result in neurodevelopmental disorders and retardation syndromes (2). It is recognized that not only the steady-state level of cholesterol is critical for brain function but also its constant turnover (3, 4). Much of brain cholesterol is found in myelin sheaths of oligodendrocytes surrounding the axons of neurons where it is turned over slowly (0.4% per day in mouse, 0.03% in human) (1), but a more metabolically active pool of cholesterol is located in intracellular structures such as the endoplasmic reticulum, Golgi apparatus, and nucleus of neurons. Here turnover is estimated at 20% per day in mouse (1). However, a precise map of cholesterol turnover across the specialized functional regions of brain remains to be generated.

Oxysterols are oxidized forms of cholesterol, or of its precursors, and represent the initial metabolites in cholesterol catabolism (5). One of the most well-studied oxysterols in brain is 24S-hydroxycholesterol (24S-HC, see *SI Appendix*, Table S1 for abbreviations and common and systematic names). In mammals 24S-HC is mostly synthesized in neurons by the enzyme cytochrome P450 (CYP) 46A1 (cholesterol 24S-hydroxylase, CYP46A1) and acts as a transport form of cholesterol (*SI Appendix*, Fig. S1) (4, 6,

7). Unlike cholesterol, 24S-HC can cross the BBB. The oxysterol 24S-HC is a ligand to the liver X receptors (LXRs) (8), the β-form of which is highly expressed in brain (9), a potent modulator of the *N*-methyl-D-aspartate receptors (NMDARs) (10), glutamate-gated ion channels that are critical to the regulation of excitatory synaptic function in the CNS, and it is also a modulator of cholesterol biosynthesis by interacting with the endoplasmic reticulum protein INSIG (insulin induced gene) and restricting transport and processing of SREBP-2 (sterol regulatory element-binding protein-2) to its active form as a master transcription factor for cholesterol biosynthesis (11). Despite its potent biological activity, little is known about levels of 24S-HC in distinct regions of brain (12, 13). This is also true of 24S,25-epoxycholesterol (24S,25-EC), which is formed via a shunt pathway of cholesterol biosynthesis in parallel to the Bloch pathway but without the involvement of 24-dehydrocholesterol reductase (DHCR24, *SI Appendix*, Fig. S1) (14, 15). The oxysterol 24S,25-EC has also been shown to be formed from desmosterol by CYP46A1 in vitro (16). It is a potent activator of the LXRs, inhibitor of SREBP-2 processing, and also a ligand to the G protein-coupled receptor (GPCR) Smoothened (SMO), a key protein in the Hedgehog (Hh) signaling pathway (8, 11,

Significance

The brain is a remarkably complex organ and cholesterol homeostasis underpins brain function. It is known that cholesterol is not evenly distributed across different brain regions; however, the precise map of cholesterol metabolism in the brain remains unclear. If cholesterol metabolism is to be correlated with brain function it is essential to generate such a map. Here we describe an advanced mass spectrometry platform to reveal spatial cholesterol metabolism in situ at 400-µm spot diameter on 10-µm tissue slices from mouse brain. We mapped, not only cholesterol, but also other biologically active sterols arising from cholesterol turnover in both wild type and mice lacking cholesterol 24S-hydroxylase (CYP46A1), the major cholesterol metabolizing enzyme.

BIOCHEMISTRY

17, 18). The oxysterol 24S,25-EC has been shown to be important in dopaminergic neurogenesis via activation of LXRs (19, 20).

The cholestenoic acids, 3β,7α-dihydroxycholest-5-en-(25R)26-oic (3β,7α-diHCA) and 7α-hydroxy-3-oxocholest-4-en-(25R)26-oic (7αH,3O-CA) acids, also formed by enzymatic oxidation of cholesterol, are found in cerebrospinal fluid (CSF), the fluid that bathes the CNS (21, 22). The acid 7αH,3O-CA has been suggested to provide an export route for (25R)26-hydroxycholesterol (26-HC, also called 27-hydroxycholesterol) which itself passes into the brain from the circulation, but does not accumulate in brain (*SI Appendix*, Fig. S1) (23, 24). The acid 3β,7α-diHCA has been shown to be biologically active as a ligand to the LXRs and to be protective toward oculomotor neurons (21). The location of the acid has not previously been defined in brain (25).

To understand better the importance in brain of sterols in general, and oxysterols in particular, it is necessary to correlate molecular concentrations with histology. This can be achieved by exploiting mass spectrometry imaging (MSI). MSI technology mostly utilizes matrix-assisted laser desorption/ionization (MALDI)-MS (26–29). MALDI-MSI has been used to image lipids in brain (30–32); however, cholesterol and other sterols tend to be poorly ionized by conventional MALDI and are underrepresented in MALDI-MSI studies. To enhance ionization, other desorption/ionization methods have been employed, including nanostructure-initiator MS (33), sputtered silver-MALDI (34), and silver nanoparticle-MALDI (35). These studies are mainly restricted to cholesterol. Alternatively, on-tissue derivitization has been used to enhance MS ionization and to image steroid hormones and steroidal drugs in tissue by exploiting hydrazine reactions with carbonyl groups present in target analytes (36–41). These derivatives have been used in combination with MALDI and with liquid extraction for surface analysis (LESA) technology, or with reactive-DESI (desorption electrospray ionization) (36, 42). Hydrazine derivatization is problematic for sterols, oxysterols, or steroids not possessing a carbonyl group. To address this issue, for in-solution analysis of oxysterols and sterols, we and others have utilized a bacterial cholesterol oxidase enzyme to specifically convert sterols with a 3β-hydroxy-5-ene structure to a 3-oxo-4-ene and then derivatize the resulting 3-oxo group with the Girard hydrazine reagent to provide a charge-tag to the target molecule (Fig. 1) (43–45). This strategy is termed enzyme-assisted derivatization for sterol analysis (EADSA). For comprehensive analysis, oxysterols naturally possessing an oxo group, e.g., 7αH,3O-CA or 7-oxocholesterol (7-OC, also called 7-ketocholesterol)

can be derivatized in parallel in the absence of cholesterol oxidase (Fig. 1).

In the current study we describe how on-tissue EADSA with microscale-LESA (μLESA) and liquid chromatography (LC)-MS can be exploited for the localization of cholesterol, its precursors, and metabolites, in rodent brain. The incorporation of online LC is essential to separate isomers and also low-abundance sterols from dominating cholesterol. We find 24S-HC to be the most abundant oxysterol in all brain regions, being at the highest levels in striatum and thalamus and at the lowest levels in gray matter of cerebellum. The oxysterol 24S,25-EC is also abundant in thalamus and sparse in gray matter of cerebellum. We are able to definitively identify 3β,7α-diHCA in brain, where it is most abundant in gray matter of the cerebellum. We confirm that 24S-HC is almost completely absent from brain of the *Cyp46a1* knockout mouse (*Cyp46a1*$^{-/-}$). The level of 24S,25-EC is reduced in the *Cyp46a1*$^{-/-}$ mouse but low levels of 20S-hydroxycholesterol (20S-HC), 22R-hydroxycholesterol (22R-HC), 24R-hydroxycholesterol (24R-HC), and 25-hydroxycholesterol (25-HC) are present in this mouse.

Results

Development of the Analytical Platform.
The platform was designed to allow the localization by MS of cholesterol, its immediate precursors, and of multiple oxysterols in tissue against a large background of cholesterol and other more readily ionized lipids. To meet this challenge, we have used on-tissue derivatization (Fig. 1) in combination with μLESA and LC-MS with multistage fragmentation (MS^n). Each of the system components required optimization as described below.

On-Tissue EADSA.
The protocol for on-tissue enzymatic oxidation of sterols (Fig. 1*B*) was adapted from the in-solution procedure using cholesterol oxidase enzyme in KH$_2$PO$_4$ buffer (43, 45), the only difference being that the enzyme was sprayed onto tissue in buffer and then incubated at 37 °C in a humid chamber (11.9 cm × 8.2 cm × 8.5 cm, 30 mL water), rather than being in solution. In trial experiments, after a 1-h incubation period at 37 °C there was no evidence for any nonoxidized sterol, as indicated by an absence of peaks corresponding to [M+H]$^+$, [M+Na]$^+$, [M+K]$^+$, [M+H-(H$_2$O)$_n$]$^+$, [M+Na-(H$_2$O)$_n$]$^+$ or [M+K-(H$_2$O)$_n$]$^+$ of endogenous cholesterol or 24S-HC, or of added deuterated standards, only of the 3-oxo-4-ene oxidation products (see also *SI Appendix*). The next step in the method was on-tissue derivatization of oxo-containing sterols using the Girard P (GP) hydrazine reagent (Fig. 1). Others have used Girard T (GT) hydrazine as the derivatizing agent to react on-tissue with oxo-containing sterols/steroids (36–41); however, based on our experience of using the GP reagent for in-solution derivatization of oxysterols, GP hydrazine was preferred here (43, 45). A disadvantage of using GT hydrazine is that a major MS^2 fragment ion is the [M-59]$^+$ species ([M-NMe$_3$]$^+$) and the exact same neutral loss is observed in the fragmentation of endogenous choline-containing lipids. With [^{2}H$_0$]GP the major MS^2 fragment ion is [M-79]$^+$ and for [^{2}H$_5$]GP [M-84]$^+$, neutral losses not common for other lipids (for further details of fragmentations see refs. 25 and 43). We sprayed GP reagent (6.3 mg/mL for [^{2}H$_5$]GP bromide) in the same solvent as previously used for in-solution derivatization (70% methanol, 5% acetic acid) (43, 45). As in reported studies using the GT reagent (36, 37, 40), it was essential to incubate the GP-coated tissue in a humid atmosphere to achieve efficient derivatization. Initial tests in a dry atmosphere revealed no derivatization of 3-oxo-4-ene substrates. Incubation in a humid chamber (12 cm × 12 cm × 7.2 cm) containing 30 mL of 50% methanol, 5% acetic acid at 37 °C for 1 h provided an efficient derivatization environment with minimum lateral dispersion of analytes (*SI Appendix*, Fig. S2). Increasing the volume or organic content of solution led to lipid delocalization, while reducing the volume and organic content
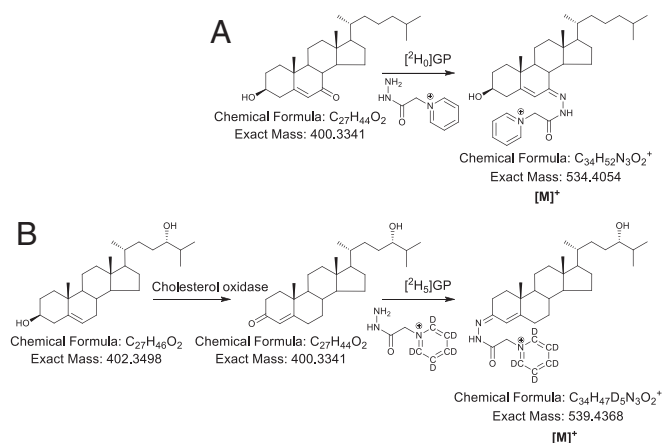
Fig. 1. Derivatization of oxysterols. (*A*) Derivatization of 7-OC with [^{2}H$_0$] Girard P reagent ([^{2}H$_0$]GP) and of (*B*) 24S-HC with [^{2}H$_5$]GP reagent following enzymatic oxidation with cholesterol oxidase. For MS^n fragmentation see refs. 25 and 43 and *SI Appendix*, Fig. S9F.

provided less efficient derivatization based on ion current in µLESA-MS measurements.

µLESA. LESA is based on liquid microjunction surface sampling (46), where solvent is deposited as a small volume liquid microjunction by a robotic sampling probe, i.e., pipette tip or capillary, onto a surface, aspirated back to the tip or capillary, and the extract analyzed by electrospray ionization (ESI)-MS. The LESA^PLUS configuration of the TriVersa Nanomate incorporates a 200-µm internal diameter (i.d.)/360-µm outer diameter (o.d.) fused silica capillary replacing the conventional pipette tip (47), reducing the extraction spot size to ≤1 mm (48, 49). However, when using a 50% methanol solvent, as required here for extraction of derivatized sterols, we were unable to achieve this spot size as the surface tension required for a stable liquid microjunction was not attainable. To overcome this problem, the sampling probe can be used to make a seal against the tissue surface, thereby minimizing the possibility of solvent spreading (50). We have attached a 330-µm i.d./794-µm o.d. FEP (fluorinated ethylene propylene) sleeve to the fused silica capillary and used it to make a direct seal with the tissue surface, preventing spreading of the extraction solvent beyond the boundary of the sleeve (*SI Appendix*, Fig. S3A). This gave a spot size diameter of ≤400 µm, as assessed by microscopic evaluation of tissue after liquid extraction was performed in triplicate (*SI Appendix*, Fig. S3B). A 50% methanol extraction solvent was chosen to closely match the derivatization solvent. The volume of solvent dispensed onto (more correctly, forced to be in contact with) tissue, was optimized to maximize oxysterol extraction with an extraction time of 30 s, as assessed by MS ion current for target oxysterols (e.g., 24S-HC), without compromising spatial resolution, i.e., leaking of solvent through the tissue–FEP seal. The number of repeat extractions on the same spot was similarly optimized. The optimal conditions were a "dispensed volume" of 1 µL, an extraction time of 30 s, and performed three times on the same spot.

EADSA-µLESA-LC-MS. Previous studies using MS have defined concentrations of 24S-HC, the major oxysterol in mouse brain, to be of the order of 20 to 60 ng/mg (wet weight) (25, 51–53). For comparison, the concentration of cholesterol is in the range of 10 to 20 µg/mg (1, 25, 52), and after EADSA treatment, in the absence of chromatographic separation, cholesterol totally dominates the µLESA-MS analysis of the mouse brain surface extract (Fig. 2A). However, with the addition of LC to give the µLESA-LC-MS platform, analysis of 400-µm diameter spot extracts of brain tissue give clear separation of peaks corresponding to 24S-HC, 24S,25-EC, desmosterol, 8(9)-dehydrocholesterol (8-DHC), and cholesterol (Fig. 2B). The 8-DHC is an enzymatically generated isomer of 7-dehydrocholesterol (7-DHC), the immediate precursor of cholesterol in the Kandutsch–Russell pathway (54).

We integrated µLESA with two different LC-MS systems: 1) µLESA-LC-MS with a "conventional" flow rate of 200 µL/min, and 2) µLESA-nano-LC-MS with a flow rate of 350 nL/min. Both systems incorporate a microswitch and a reversed-phase trap column prior to an analytical column which allowed trapping of GP-derivatized sterols and washing to waste of unreacted GP reagent and more polar analytes (*SI Appendix*, Fig. S4 A and B). The nano-LC-MS format gives a 10-fold improvement in sensitivity over the conventional flow-rate LC-MS format, based on analysis of 24S-HC, and is more suitable for the analysis of very low-abundance oxysterols; however, it is susceptible to overloading by highly abundant cholesterol. Both systems were utilized in this study to cover the broadest range of sterols in brain.

Quantification Using On-Tissue Internal Standards. To quantify sterols and oxysterols, isotope-labeled surrogates were sprayed on-tissue providing known areal densities of internal standards. Initially, the validity of using sprayed-on [^{2}H$_7$]24R/S-HC as an internal standard

for quantification of oxysterols was assessed by spraying both [^{2}H$_7$]24R/S-HC and [^{2}H$_7$]22S-HC onto six successive slices of brain tissue at increasing concentration ratios of [^{2}H$_7$]24R/S-HC: [^{2}H$_7$]22S-HC, but keeping the areal density of [^{2}H$_7$]22S-HC constant. A plot of peak area ratio of [^{2}H$_7$]24R/S-HC: [^{2}H$_7$]22S-HC (averaged over three closely arranged spots from the same isocortical region on each slice) against areal density of sprayed-on [^{2}H$_7$]24R/S-HC, gave a straight line with $R^2 > 0.999$ (*SI Appendix*, Fig. S5A). When this experiment was repeated but by plotting the peak area ratio of [^{2}H$_7$]24R/S-HC: 24S-HC, where 24S-HC refers to the endogenous molecule, against areal density of sprayed-on [^{2}H$_7$]24R/S-HC, for closely arranged spots ($n = 3$) in the same region of interest, on six successive slices, the result was a straight line of $R^2 > 0.994$ (*SI Appendix*, Fig. S5 B and C). Assuming the concentration of endogenous 24S-HC does not vary across the six slices, or adjacent spots within the same region of interest, the results indicate that deuterated surrogates can be used as a reliable internal standard for quantification of endogenous sterols.

To assess the reproducibility of the EADSA-µLESA-LC-MS technology, adjacent spots ($n = 6$) in the isocortical region of a single slice of mouse brain were analyzed. The mean value of areal density of 24S-HC was determined to be 0.947 ± 0.078 ng/mm^2 (mean ± SD), giving a % coefficient of variation (% CV) of 8%. Assuming that the endogenous concentration of 24S-HC did not vary across the six adjacent spots, the reproducibility of the method is satisfactory. Reproducibility was further assessed by analyzing nine regions of interest from four closely cut slices from a single brain. The % CV for areal density in each individual region varied from 12.4% for the striatum where the areal density of 24S-HC was high (1.415 ± 0.176 ng/mm^2, $n = 4$) to 46.3% in the white matter of the cerebellum where the areal density of 24S-HC was low (0.191 ± 0.088 ng/mm^2, $n = 4$, *SI Appendix*, Fig. S6A). However, there is likely some contamination of white matter of the cerebellum by gray matter and vice versa, accounting for the high % CV in these regions. Other than for the cerebellum, the interslice reproducibility was deemed acceptable. Similar analysis for cholesterol with conventional LC-MS gave a value of 387.3 ± 14.6 ng/mm^2 (% CV = 4%) for five adjacent spots in the isocortex of a single tissue slice.

Cholesterol Metabolism in Different Regions of Wild-Type Mouse Brain. Although cholesterol has been imaged in adult rodent brain, its precursors and metabolites have not. To demonstrate the potential of our platform and gain insight into spatial cholesterol metabolism in brain, we quantitatively analyzed the sterol distribution in nine regions of interest, i.e., isocortex, striatum, thalamus, hippocampus, midbrain, pons, medulla, cerebellum (gray matter), and cerebellum (white matter) using µLESA-LC-MS with conventional-flow and nano-LC-MS formats (Fig. 3).

Cholesterol is the most abundant sterol across the whole brain but there are concentration differences between regions (Figs. 3A and 4A). Hierarchal cluster analysis separated the nine regions into three groups (Fig. 4B), of which cholesterol is most abundant in pons (575.5 ± 122.0 ng/mm^2, $n = 3$ animals) and white matter of the cerebellum (509.2 ± 83.0 ng/mm^2) but least abundant in hippocampus (252.9 ± 27.3 ng/mm^2), gray matter of cerebellum (263.3 ± 71.3 ng/mm^2), and isocortex (305.1 ± 53.8 ng/mm^2). Desmosterol, the immediate precursor of cholesterol in the Bloch pathway, was found to be about two orders of magnitude less abundant than cholesterol but its spatial distribution correlated significantly with cholesterol (*SI Appendix*, Fig. S7A). The areal density of desmosterol ranged from 4.212 ± 1.546 ng/mm^2 in pons to 1.025 ± 0.356 ng/mm^2 in the gray matter of the cerebellum (Figs. 3B and 4C). We also detected 8-DHC in our analysis (Fig. 2 B and E), which is an enzymatic isomeric product 7-DHC, the immediate precursor of cholesterol in the Kandutsch–Russell pathway (*SI Appendix*, Fig. S1) (54). The
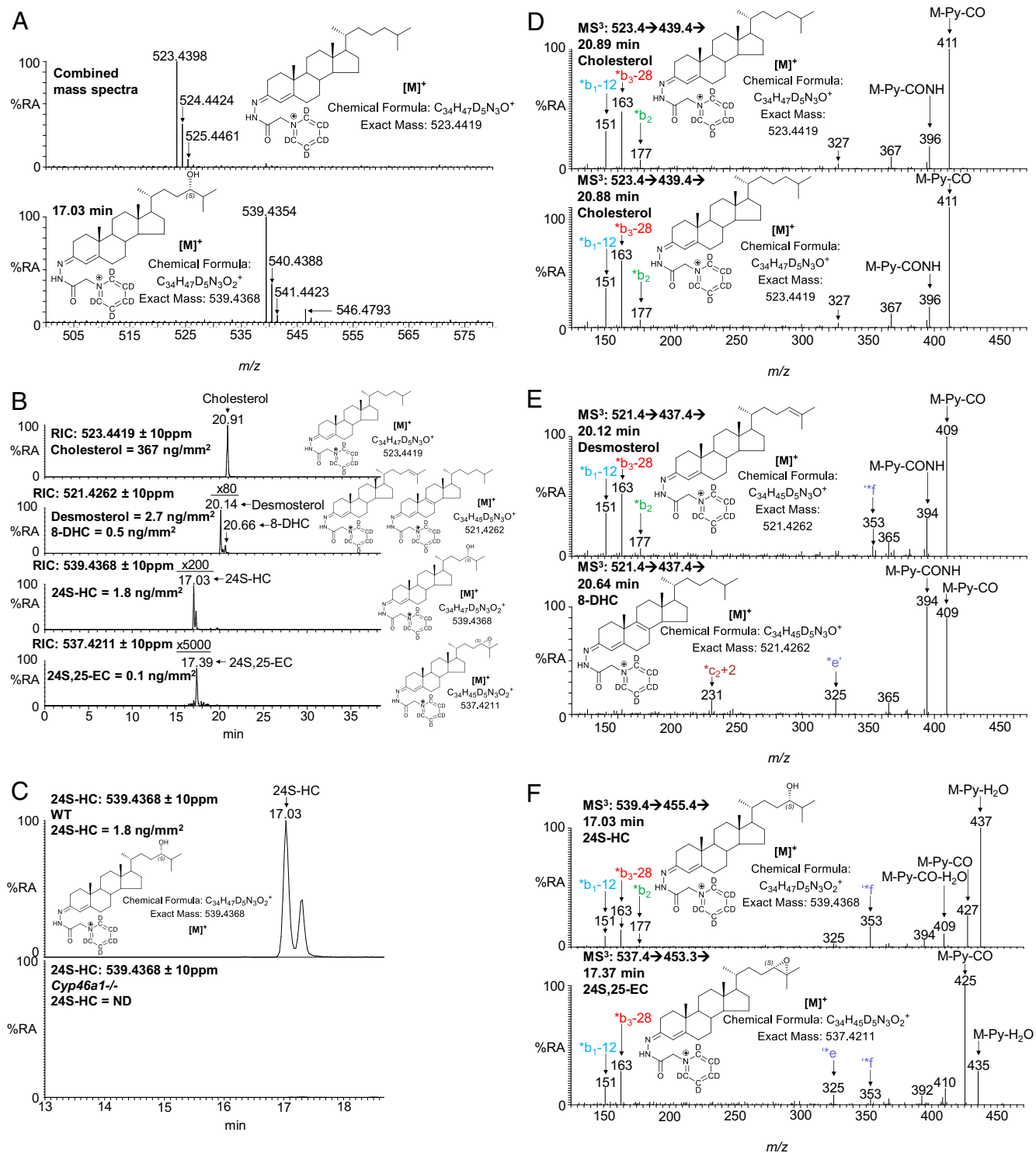
Fig. 2. μLESA-LC-MS(MSⁿ) analysis following EADSA treatment of mouse brain. (*A, Upper*) Combined mass spectra recorded over the entire chromatogram, from striatum of WT mouse brain. (*A, Lower*) Mass spectrum recorded at 17.03 min from the same brain region. The peaks at *m/z* 523.4398, 539.4354, and 546.4793 correspond to endogenous cholesterol, 24S-HC and [²H₇]24S-HC internal standard, respectively. (*B*) RICs for the [M]⁺ ion of endogenous cholesterol (*m/z* 523.4419 ± 10 ppm, *Upper*), dehydrocholesterols (521.4262 ± 10 ppm, second panel), 24S-HC (539.4368 ± 10 ppm, third panel) and 24S,25-EC (537.4211 ± 10 ppm, *Lower*) from striatum of WT mouse brain. Peak intensities are relative to cholesterol but magnified as indicated. (*C*) RIC for the [M]⁺ ion of endogenous 24S-HC (*m/z* 539.4368 ± 10 ppm) from striatum of WT brain (*Upper*) and of *Cyp46a1⁻/⁻* mouse brain (*Lower*). Peak intensities are normalized to the 24S-HC peak from WT mouse brain. ND, not detected. Note, 24S-HC appears as a doublet in chromatograms in *B* and *C*, this is a consequence of *syn* and *anti* conformers of the GP derivative. (*D*) MS³ ([M]⁺ → [M-Py]⁺→) spectra recorded at 20.89 min and 20.88 min corresponding to endogenous cholesterol from two consecutive spots in the striatum. (*E*) MS³ ([M]⁺ → [M-Py]⁺→) spectra recorded at 20.12 min corresponding to endogenous desmosterol (*Upper*) and 20.64 min corresponding to 8-DHC (*Lower*) from striatum of WT mouse. (*F*) MS³ ([M]⁺ → [M-Py]⁺→) spectra recorded at 17.03 min corresponding to endogenous 24S-HC (*Upper*) and 17.37 min corresponding to 24S,25-EC (*Lower*) from striatum of WT mouse. Note in the EADSA process 24S,25-EC isomerizes to 24-oxocholesterol.
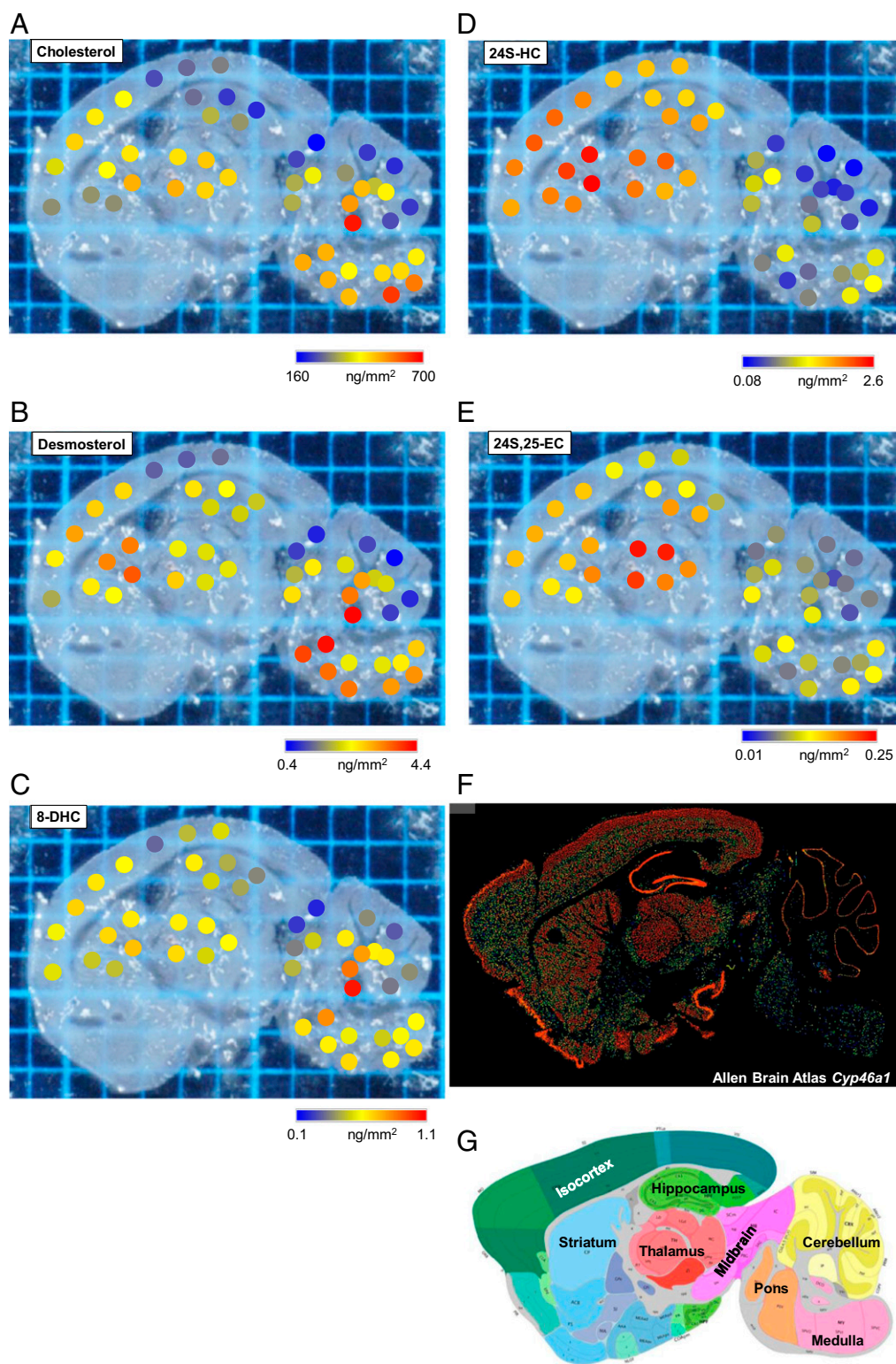
Fig. 3. Sagittal section of a WT mouse brain analyzed by μLESA-LC-MS following EADSA treatment. A photograph of a tissue slice showing spots analyzed with areal density, determined by μLESA-LC-MS, of (*A*) cholesterol, (*B*) desmosterol, (*C*) 8-DHC, (*D*) 24S-HC, and (*E*) 24S,25-EC. Areal density is color coded on a blue-to-red scale as indicated. (*F*) Expression of *Cyp46a1* (55). Image courtesy of © 2006 Allen Institute for Brain Science. Mouse Brain. Available from: https://mouse.brain-map.org/experiment/show/532667. (*G*) Annotation of the different regions of mouse brain (55). Image courtesy of © 2006 Allen Institute for Brain Science. Mouse Brain. Available from: http://mouse.brain-map.org/experiment/thumbnails/100042147?image_type=atlas.

areal density of 8-DHC was consistently lower than that of desmosterol in all brain regions measured, but its distribution pattern is quite similar to that of desmosterol and cholesterol (Figs. 3 and 4). These data indicate that the distributions of cholesterol and its immediate precursors are correlated together in brain (*SI Appendix*, Fig. S7A).
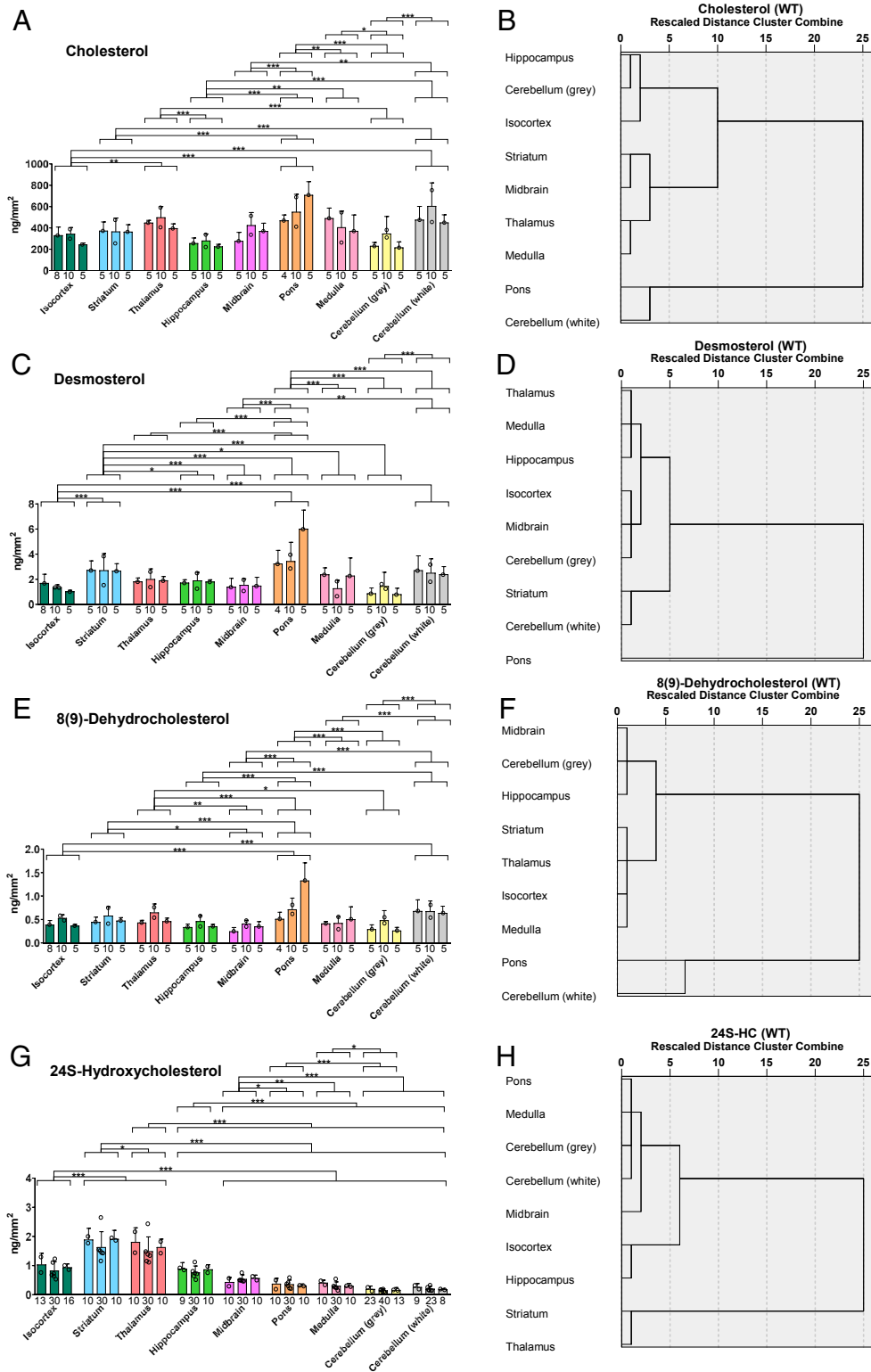
Fig. 4. Sagittal section of WT mouse brain analyzed by μLESA-LC-MS following EADSA treatment. Areal density (ng/mm^2) of sterols in nine brain regions from three WT mice and dendrograms from hierarchal cluster analysis for the brain regions averaged over the biological replicates (see *Statistics* section). Areal density of (*A*) cholesterol, (*C*) desmosterol, (*E*) 8-DHC, and (*G*) 24S-HC. Significance levels from ANOVA using Tukey's multiple comparison test are indicated for those brain regions showing significant differences. *$P < 0.05$, **$P < 0.01$, ***$P < 0.001$. Values for individual mice are given by separate histogram bars. The number of dots within each bar indicates the number of brain slices analyzed for each mouse. The dots within the bars correspond to region average for each brain slice. The height of each bar represents the mean of the region average of each brain slice. The number at the bottom of each bar indicates the total number of spots analyzed per mouse. The error bars indicate the SD of all of the spots per mouse. Dendrograms for (*B*) cholesterol, (*D*) desmosterol, (*F*) 8-DHC, and (*H*) 24S-HC. A greater horizontal axis distance from zero indicates greater dissimilarity between different brain regions, whereas a lower distance from zero indicates greater similarity between different brain regions.

The major cholesterol metabolite in brain is 24S-HC, accounting for around 50% of cholesterol turnover in the brain. However, the distribution of 24S-HC is significantly different across different brain structures (Figs. 3D and 4G), ranging in areal density from 0.161 ± 0.024 ng/mm^2 in the gray matter of the cerebellum to 1.637 ± 0.159 ng/mm^2 in the thalamus and 1.805 ± 0.158 ng/mm^2 in the striatum. Remarkably, the distribution of 24S-HC across the different brain regions does not correlate significantly with levels of cholesterol or its precursors (SI Appendix, Fig. S7A). Interestingly, while the level of 24S-HC varies by a factor of about 10 across the different regions, the corresponding variations of cholesterol and desmosterol are only factors of about 2 and 4, respectively. The oxysterol 24S-HC is formed from cholesterol by the enzyme CYP46A1 expressed in neurons localized to multiple subregions of brain (6). Interrogation of the Allen Mouse Brain Atlas reveals that Cyp46a1 is highly expressed in striatum and thalamus but at lower levels in the cerebellum (Fig. 3F) (55). Our results suggest that the pattern of 24S-HC in brain reflects local Cyp46a1 expression.

Another oxysterol identified in brain is 24S,25-EC (Fig. 2 B and F) (15). This oxysterol is not a metabolite of cholesterol, but formed in parallel to cholesterol via a shunt pathway using the exact same enzymes, but with the exclusion of DHCR24 (SI Appendix, Fig. S1) (14). In cellular systems, the level of 24S,25-EC reflects the activity of the cholesterol biosynthesis pathway. Recent studies also suggests that 24S,25-EC can be formed in vitro from desmosterol via a CYP46A1 catalyzed reaction (16). We found 24S,25-EC to be present in all brain region but to be particularly abundant in thalamus at an areal density of 0.158 ± 0.026 ng/mm^2 (Figs. 3E and 5A). Factor analysis reveals that 24S,25-EC correlates most closely with 24S-HC (SI Appendix, Fig. S7A), although being about 10 times less abundant. The distribution of 24S,25-EC in brain likely reflects the varying activities of de novo cholesterol biosynthesis and of CYP46A1 in the different brain regions.

While, cholesterol, desmosterol, 8-DHC, 24S-HC, and 24S,25-EC can all be analyzed by EADSA-µLESA-LC-MS at conventional flow rates, low-abundance oxysterols require the more sensitive EADSA-µLESA-nano-LC-MS format. The nano-LC-MS format provides a lower limit of quantification (LOQ) of 0.01 ng/mm^2 based on a CV of <25% at the LOQ and a limit of detection (LOD) of 0.001 ng/mm^2 (SI Appendix, Fig. S5).

Previous studies have suggested that 26-HC is imported into brain and converted in brain by a combination of enzymes, CYP27A1, and CYP7B1 to 3β,7α-diHCA and further by hydroxysteroid dehydrogenase (HSD) 3B7 to 7αH,3O-CA (SI Appendix, Fig. S1) (21, 23, 24, 56). The acid 3β,7α-diHCA is a ligand to the LXRs and is neuroprotective, while 7αH,3O-CA lacks these activities (21). Using EADSA-µLESA-nano-LC-MS, 3β,7α-diHCA and 7αH,3O-CA are detected in brain. However, using the EADSA method, 3β,7α-diHCA can be measured in combination with 7αH,3O-CA, and at low levels the combined areal densities of these two acids are measured more accurately than either of the individual acids alone. The combination of 3β,7α-diHCA plus 7αH,3O-CA was evident at areal densities ranging from close to the LOD, i.e., 0.002 ± 0.002 ng/mm^2 up to 0.018 ± 0.009 ng/mm^2 across the different regions of interest in mouse brain (SI Appendix, Table S1). The combined acids were found to be most abundant in the gray matter of the cerebellum, although not statistically different from the white matter of the cerebellum or isocortex (Fig. 5G and see also SI Appendix, Table S1).

The oxysterol 7-OC can be formed from 7-DHC in a CYP7A1 catalyzed reaction (57), or alternatively, from cholesterol via free radical-mediated reactions (58). As CYP7A1 is not expressed in brain, free radical formation or import across the BBB are the likely origins of this oxysterol in brain. The oxysterol 7-OC has previously been detected in brain using Girard derivatization

(36). We find it to be distributed ubiquitously across the brain at low levels (0.002 ± 0.002 to 0.004 ± 0.006 ng/mm^2, see SI Appendix, Fig. S8).

Taken together, using EADSA-µLESA-LC-MS data we clearly demonstrate that different brain regions have distinct sterol patterns.

Locating Biologically Active Oxysterols in Cyp46a1$^{-/-}$ Mouse Brain. Earlier studies have shown that although converting cholesterol to 24S-HC by CYP46A1 is responsible for the majority of cholesterol turnover in brain, the cholesterol content of whole brain does not differ significantly between wild-type (WT) and Cyp46a1$^{-/-}$ animals (52, 53, 59). This was explained by a reduction of cholesterol synthesis compensating for reduced metabolism in the Cyp46a1$^{-/-}$ animals. As 24S,25-EC levels in brain may reflect the combined activities of de novo cholesterol synthesis and CYP46A1, we hypothesized that the levels of 24S,25-EC are reduced in Cyp46a1$^{-/-}$ mice. Indeed, we found that the level of 24S,25-EC decreased in all brain regions analyzed. In particular, the areal densities of 24S,25-EC in the thalamus and striatum of Cyp46a1$^{-/-}$ animals were reduced by about 80 to 90% compared to WT brain (Fig. 5 A and C and SI Appendix, Table S1), while there was only about a 50% reduction in medulla and cerebellum, demonstrating that a lack of CYP46A1 reduced 24S,25-EC in brain and that the thalamus and striatum are the most affected areas. Notably, the dendrograms from hierarchal cluster analysis are different in the two genotypes (Fig. 5 B and D).

In the WT mouse, the high areal density of 24S-HC (0.161 ± 0.024 to 1.805 ± 0.158 ng/mm^2) compared to other oxysterols makes the identification of minor (≤ 0.01 ng/mm^2) and closely eluting monohydroxycholesterols difficult. To overcome this problem, we have taken advantage of brain tissue from the Cyp46a1$^{-/-}$ mouse which is reported to be almost completely devoid of 24S-HC (52, 53, 59). Analysis of the same brain regions as for WT mouse confirmed an almost complete absence (≤ 0.001 ng/mm^2) of 24S-HC in the Cyp46a1$^{-/-}$ animal (Fig. 2C and see also SI Appendix, Table S1) but revealed minor amounts of 25-HC (0.005 ± 0.002 to 0.023 ± 0.034 ng/mm^2) and 24R-HC (0.004 ± 0.002 to 0.023 ± 0.001 ng/mm^2, SI Appendix, Fig. S9). Although there was some variation in absolute concentrations in different mice, 24R-HC was at the highest concentration in the cerebellum of each mouse (Fig. 5E and see also SI Appendix, Table S1) and 25-HC was more ubiquitously dispersed (SI Appendix, Fig. S8 and Table S1). Both of these oxysterols were detected at low levels in an earlier study of homogenized Cyp46a1$^{-/-}$ mouse brain, as was an unknown hydroxycholesterol eluting later than the peaks of 24R-HC (52). Here we again observe low levels of this oxysterol (0.007 ± 0.005 to 0.012 ± 0.006 ng/mm^2) which we have previously assigned, based on retention time and MS^3 spectra, but in the absence of an authentic standard, to be 12α-hydroxycholesterol (12α-HC, SI Appendix, Fig. S9 A and E) (25).

Careful interrogation of the MS^3 spectra recorded prior to the elution of 25-HC indicate the presence of not only trace quantities of 24S-HC (at about the limit of detection, SI Appendix, Fig. S9 A and C), but also of the elusive 20S-HC (SI Appendix, Fig. S9B) (60). The oxysterol 20S-HC gives a unique MS^3 spectrum where the fragment ion m/z 327.2 is abundant (SI Appendix, Fig. S9 B and F). By generating a multiple reaction monitoring (MRM) chromatogram for the transition m/z 539.4 → 455.4 → 327.2, this oxysterol is highlighted (SI Appendix, Fig. S9A). When the authentic standard of GP-derivatized 20S-HC was spotted on mouse brain tissue, it eluted with an identical retention time to the GP-derivatized endogenous molecule, and the MS^3 spectra of the standard and endogenous molecule are almost identical. There are some small differences as a consequence of partial coelution of isomeric oxysterols from tissue.

However, an intense fragment ion at m/z 327.2 is unique to 20S-HC. The oxysterol 20S-HC is a ligand of SMO and can activate the Hh signaling pathway and has previously been reported in only one prior publication, where it was found to be present in rat brain and human placenta (61). Here we define its presence in mouse brain. Our data demonstrate that 20S-HC is
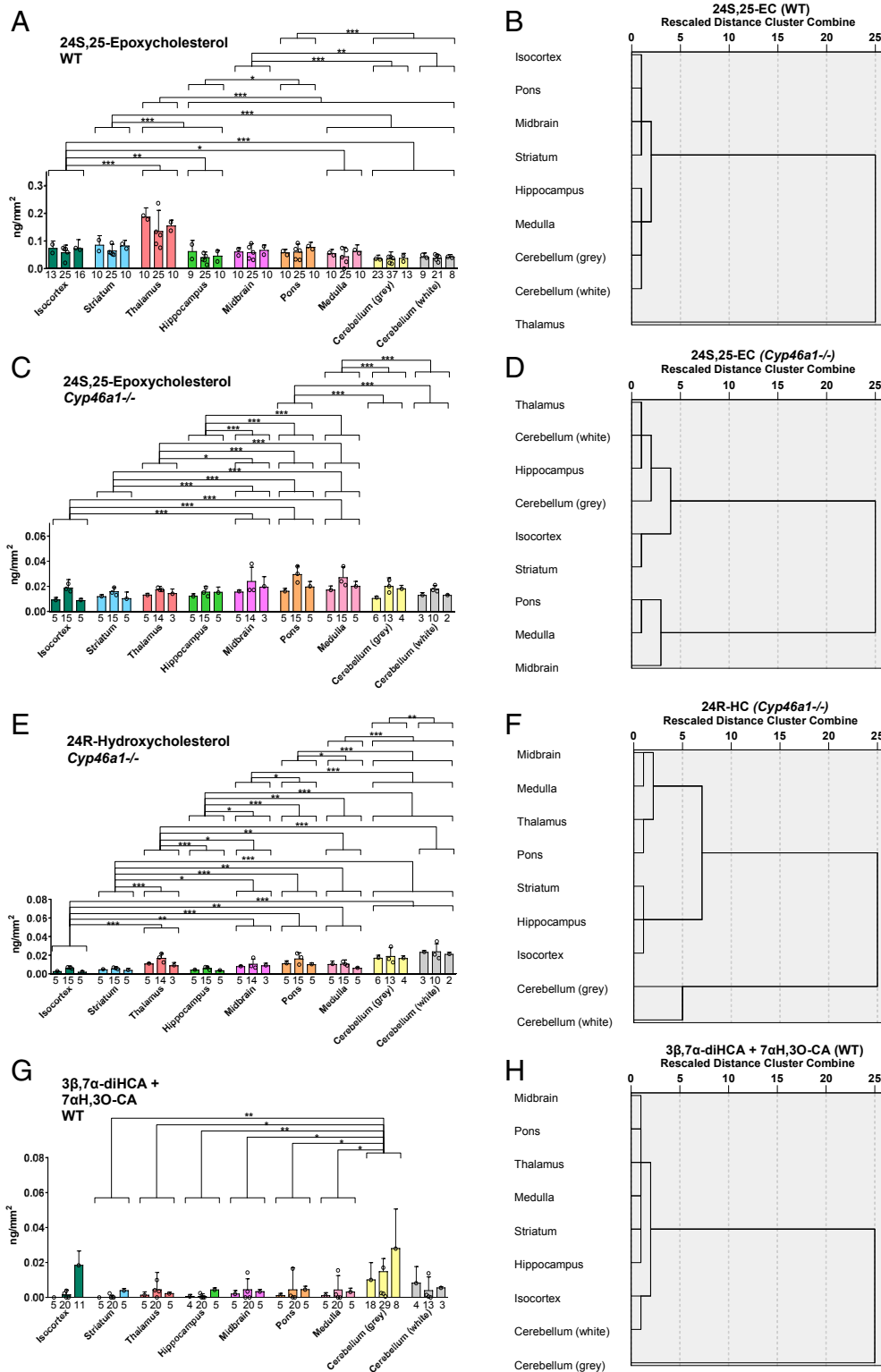

Fig. 5. Sagittal section of WT and $Cyp46a1^{-/-}$ mouse brain analyzed by µLESA-LC-MS following EADSA treatment. Areal density (ng/mm²) of sterols in nine brain regions from three mice of each genotype and dendrograms from hierarchal cluster analysis for the brain regions averaged over the biological replicates. Areal density of (A) 24S,25-EC, WT mouse; (C) 24S,25-EC, $Cyp46a1^{-/-}$ mouse; (E) 24R-HC, $Cyp46a1^{-/-}$ mouse; and (G) combined 3β,7α-diHCA and 7αH,3O-CA, in WT mouse. Statistical analysis and labeling is as described in Fig. 4. *$P < 0.05$, **$P < 0.01$, ***$P < 0.001$. Dendrograms for (B) 24S,25-EC, WT mouse; (D) 24S,25-EC, $Cyp46a1^{-/-}$ mouse; (F) 24R-HC, $Cyp46a1^{-/-}$ mouse; and (H) combined 3β,7α-diHCA and 7αH,3O-CA, in WT mouse.

ubiquitously distributed in brain regions at an areal density of about 0.004 ± 0.003 to 0.007 ± 0.003 ng/mm^2 in $Cyp46a1^{-/-}$ mice (*SI Appendix*, Fig. S8 and Table S1).

As discussed above, the combined areal densities of 3β,7α-diHCA and 7αH,3O-CA (*SI Appendix*, Fig. S8) can be measured more accurately than either of the individual acids alone. In agreement with the data for WT mice, the combined acids were consistently most abundant in the gray matter of the cerebellum of the $Cyp46a1^{-/-}$ mice (0.013 ± 0.014 ng/mm^2, *SI Appendix*, Fig. S8), although there was some mouse-to-mouse variation in areal density.

Cholest-4-en-3-one has been found to be present in brain of Alzheimer's disease sufferers and at lower levels in control brain samples (62). Here we detect cholest-4-en-3-one in all regions of mouse brain at areal densities in the region of 0.156 to 0.318 ng/mm^2 in both WT and $Cyp46a1^{-/-}$ animals (*SI Appendix*, Fig. S8).

Application of MALDI-MSI for Cholesterol Analysis. As an alternative to μLESA-LC-MS for the MS analysis of cholesterol, we have explored the possibility of exploiting MALDI-MSI. Using on-tissue EADSA in a similar manner to that employed with μLESA, it was possible to image the [M]$^+$ ion of GP-derivatized cholesterol (*SI Appendix*, Fig. S10). There is good visual agreement between *SI Appendix*, Fig. S10 and Fig. 4*A*.

Discussion

In the current work we have defined a methodology to locate sterols, including cholesterol, its immediate precursors, and different oxysterols in mouse brain using EADSA and μLESA-LC-MS. This method compliments MALDI-MSI methods, also based on EADSA, being concurrently developed for cholesterol imaging in the W.J.G. and Y.W. laboratory in Swansea. The μLESA-LC-MS method has a major advantage in that isomeric sterols and oxysterols can be separated by LC, even at the stereochemical level, something that has not been possible by any other separation devices linked to MS. μLESA-LC-MS technology can be operated at conventional LC flow rates for rapid analysis or on a nano-LC-MS format to achieve high sensitivity for less abundant, but biologically important oxysterols. Note, that although an oxysterol may be minor in concentration, the metabolic pathway of which it is an intermediate may be significant. The major oxysterol in brain is 24S-HC (7, 63). Here we find 24S-HC to be most abundant in the striatum and thalamus and least abundant in the cerebellum. Unsurprisingly in the WT mouse, hierarchal cluster analysis for 24S-HC reveals that striatum and thalamus cluster together, as do gray and white matter of the cerebellum with pons and medulla (Fig. 4*H*). The oxysterol 24S-HC is formed from cholesterol by the enzyme CYP46A1 expressed in neurons localized to multiple subregions of brain (6). $Cyp46a1$, is highly expressed in striatum and thalamus but at lower levels in the cerebellum (Fig. 3*F*) (55), which reflects the abundance patterns of 24S-HC, and partially of 24S,25-EC, determined here by EADSA-μLESA-LC-MS. The agreement between gene expression and enzyme product data evident here also indicates that 24S-HC does not rapidly move into other brain regions following its formation. In most studies, 24S-HC is analyzed in whole brain homogenates being found at concentrations of 20 to 60 ng/mg (wet weight). Our values of 0.161 to 1.805 ng/mm (*SI Appendix*, Table S1) translate to 16 to 176 ng/mg, assuming efficient extraction from the 10-μm thick tissue sections and minimal desiccation during tissue storage.

Cholesterol is the most abundant sterol in brain, being two to three orders of magnitude more abundant that 24S-HC. In the absence of derivatization, or chelation with Ag$^+$, cholesterol can be difficult to detect in MSI experiments (29). However, following EADSA, cholesterol provides the most intense signal in MS analysis of brain tissue (Fig. 2*A*). Cholesterol is found to be most abundant in the pons and white matter of the cerebellum (Figs. 3*A* and 4*A*); unsurprisingly, these two regions group together according

to hierarchal cluster analysis (Fig. 4*B*). Desmosterol, the immediate precursor of cholesterol in the Bloch pathway is most abundant in pons, as is 8-DHC, the isomer of 7-DHC the immediate precursor of cholesterol in the Kandutsch–Russell pathway (Figs. 3 *B* and *C* and 4 *C* and *E*). Factor analysis by sterol to sterol correlates cholesterol, desmosterol, and 8-DHC most strongly (*SI Appendix*, Fig. S7*A*). On the other hand, 24S-HC correlates most strongly with 24S,25-EC. It is noteworthy that CYP46A1 generates 24S-HC from cholesterol and 24S,25-EC from desmosterol, providing one of the two pathways to biosynthesis of 24S,25-EC. Factor analysis clusters pons and white matter of the cerebellum together, reflecting their high abundance of cholesterol and its precursors (*SI Appendix*, Fig. S7*B*). Similarly, thalamus and striatum cluster together, reflecting the abundance of 24S-HC and 24S,25-EC.

It is interesting to compare the distribution of sterols and the more abundant oxysterols with the expression of genes coding for their biosynthetic enzymes, as detailed in the Allen Mouse Brain Atlas (55). The Allen Mouse Brain Atlas (55) shows high expression in pons of 3-hydroxy-3-methylglutaryl-CoA synthase 1 (*Hmgcs1*), stearol-C-5 desaturase (*Sc5d*), *Dhcr24*, and dehydrocholesterol reductase 7 (*Dhcr7*), coding a key enzyme in the early part of the cholesterol biosynthesis pathway and three of the final enzymes in the pathway, respectively. There is also comparatively weak expression of *Cyp46a1*, coding cholesterol 24S-hydroxylase, in pons (55), which in combination can explain the elevated abundance of cholesterol in this region. According to the Allen Mouse Brain Atlas the expression of *Cyp27a1*, the gene coding the enzyme required to introduce a hydroxy and then a carboxylate group at C-26 of cholesterol, is of highest expression in the cerebellum (55), which is in agreement with data generated here, finding cholestenoic acids to be most abundant in cerebellum (Fig. 5*G*).

A point of consideration is whether residual blood in the excised brain tissue may undermine MS studies. For mouse brain it is estimated that the residual blood content can be of the order of 1% (mL/g) of the wet weight of brain (64). Taking data from ref. 25, the concentration of nonesterified 24S-HC in mouse plasma is about 5 ng/mL and in homogenized brain about 25 μg/g, so a small amount of residual blood should have little or no effect on MS data. This should also be true for cholesterol where the respective concentrations for the nonesterified molecule are 200 μg/mL and 20 mg/g, and also for 24S,25-EC (1 ng/mL cf 1 μg/g) (25). Further evidence against residual blood impacting on the data presented here, is that neither nonesterified 26-HC, abundant in mouse plasma (10 ng/mL), or 3β-hydroxycholest-5-en-(25R)26-oic acid (4 ng/mL) (25) were detected in either WT or $Cyp46a1^{-/-}$ mouse brain by MS. However, in cases where the sterol concentrations in plasma are much higher than those determined in brain, as may be the case with plant stanols and sterols, data must be interpreted with caution.

The oxysterol 24S-HC is by far the most abundant oxysterol in mouse brain (25, 52, 53). This makes analysis of closely eluting low-abundance isomers challenging. However, deletion of $Cyp46a1$ removes the biosynthesis of 24S-HC almost completely and, with implementation of nano-LC-MS, allows measurement of other isomers and oxysterols (52). In the current study we were able to image 24R-HC, the epimer of 24S-HC, which is found to be of most abundance in cerebellum (Fig. 5*E*) and to detect other isomers, including 12α-HC, 25-HC, and the elusive 20S-HC (*SI Appendix*, Fig. S8). The 22R-HC was also found in some analysis but at the limit of detection. The enzymes required to biosynthesize 24R-HC and 20S-HC from cholesterol are unknown. The enhanced abundance of 24R-HC in cerebellum of the $Cyp46a1^{-/-}$ mouse does suggest CYP27A1 to be the relevant cholesterol hydroxylase, but 24R-HC is present in brain of the $Cyp27a1^{-/-}$ mouse arguing against this (25). CYP3A11 is a sterol 24R-hydroxylase and could perhaps convert cholesterol to 24R-HC in brain. $Cyp3a11$ is, however, predominantly expressed in cortex (55). CYP11A1 is the cholesterol 22R-hydroxylase required for neurosteroid biosynthesis and has been shown to be expressed in

mouse brain (65). It first hydroxylates cholesterol at position C-22R, then at C-20, then cleaves the bond between these two carbons to generate pregnenolone. Besides being the enzyme responsible to generate 22R-HC from cholesterol, it may also be the catalyst for formation of 20S-HC from cholesterol, although evidence for this suggestion is lacking. There is only one previous report of the identification of 20S-HC in rodents or human (61). However, 20S-HC is of considerable biological interest being a ligand to the GPCR SMO, an integral receptor protein in the Hh signaling pathway, important for determining cell fate during development (66–68).

The spatial resolution and spot size available with the μLESA format (400-μm spot diameter), is admittedly inferior to that available with MALDI-MSI (<50-μm laser spot diameter). However, μLESA can be coupled with LC, offering isomer separation, essential for oxysterol analysis of tissue, where resolution of endogenous oxysterols from those generated ex vivo by oxidation in air is essential. MALDI can be linked with ion-mobility separation and MSI, but in experiments performed to date, we have been unable to separate different oxysterol isomers. A disadvantage with the μLESA-nano-LC-MS format adopted here is the length of chromatographic run time; this is however reduced by increasing LC flow rate and column diameter from a nanoscale to a more conventional scale (43, 45). However, increased flow rate does come with the penalty of reduced sensitivity, due to the concentration dependency of ESI. This is not an issue for cholesterol, desmosterol, 8-DHC, 24S-HC, or 24S,25-EC but is for less abundant oxysterols, where nano-LC-MS is more appropriate.

An alternative to μLESA is to use laser capture microdissection (LCMD) followed by conventional solvent extraction and MS to localize sterols in tissue. Such an approach has been used to investigate cholesterol localization in the retina using gas chromatography-MS following a hydrolysis step (69), and for total lipid analysis by shotgun lipidomics in mouse liver sections (70). A similar approach could be used with in-solution EADSA on captured tissue. However, as in all imaging experiments, the achievable spatial resolution of LCMD-MSI is dictated by the sensitivity of the analyzer for the target molecules. To achieve a full oxysterol profile, LCMD-MSI is likely to offer comparable results to μLESA-MS, but in the absence of robot-assisted sample handling will be more labor intensive.

MALDI-MSI has been used to image cholesterol in rodent brain with laser spot sizes of <50 μm but identification in MALDI-MSI is often based on only an [M-H$_2$O+H]$^+$ ion (71). However, with the additional application of laser-induced postionization, to give so called "MALDI-2," sensitivity is sufficient to allow spot sizes as small as 5 μm and the recording of confirmatory MS/MS spectra (72). Superior spatial resolution can be achieved using secondary ion mass spectrometry (SIMS) with spot sizes of 2 to 3 μm for the imaging of the [M-H$_2$O+H]$^+$ ion of cholesterol (73). SIMS is often linked with time-of-flight (TOF) analyzers and using TOF-SIMS, both cholesterol and cholesterol sulfate have been imaged in skin at a resolution of a few micrometers (74, 75). Even higher resolution (<0.1 μm) has been achieved with NanoSIMS to map ^{18}O isotope-labeled cholesterol in cells by monitoring the ^{18}O fragment ion (76). With respect to oxysterol analysis, however, it should be noted that oxysterols are of 10^2 to 10^3 lower abundance than cholesterol and exist as multiple positional, geometric, and stereoisomers and have yet to be imaged by TOF-SIMS or by MALDI with MS/MS.

In summary, application of EADSA with μLESA-LC-MS allows spatial location of oxysterols and cholestenoic acids in mouse brain. Through exploitation of the *Cyp46a1*$^{-/-}$ mouse, where the biosynthesis of 24S-HC is almost completely eliminated, other minor oxysterols are revealed. To compliment EADSA-μLESA-LC-MS we are developing EADSA in combination with MALDI-MSI. We find this ideal for imaging cholesterol at high spatial resolution. EADSA-MS, on a μLESA-LC-MS or MALDI-MSI format, will be a powerful tool to study specific areas of healthy and diseased tissue. As a case in point, a

recent study shows that the expression of *Cyp46a1* is decreased in the striatum of a mouse model of Huntington's disease (HD) and a gene therapy aproach to induce the expression of *CYP46A1* is suggested as a potential treatment for HD (77). An immediate application of EADSA-μLESA-LC-MS could be to assess the changes in 24S-HC, 24S,25-EC, desmosterol, and cholesterol in pathological niches in animal models of HD, and human postmortem tissues, and to monitor the production and distribution of 24S-HC in brain as a result of adeno-associated virus-mediated delivery of *CYP46A1* into mouse striatum.

Materials and Methods

Experimental Design. The objective of the current study was to develop an MS method suitable for the low-level quantitative determination of different sterols and oxysterols, including cholestenoic acids, in different regions of mouse brain. See *SI Appendix, Materials and Methods* for details of chemical reagents and tissue sectioning. All animal experiments were approved by Case Western Reserve University's Institutional Animal Care and Use Committee and conformed to recommendations made by the American Veterinary Association Panel on Euthanasia.

Deposition of Internal Standard and On-Tissue EADSA. Frozen tissue sections (10 μm) were dried in a vacuum desiccator for 15 min after which an internal standard mixture of [^{2}H$_7$]24R/S-HC (5 ng/μL), [^{2}H$_7$]22S-HC (1 ng/μL), [^{2}H$_7$]22S-HCO (1 ng/μL), in some experiments [^{2}H$_7$]22R-HCO (1 ng/μL), [^{2}H$_7$]cholesterol (20 ng/μL), and [^{2}H$_6$]desmosterol (5 ng/μL), in ethanol, was sprayed from a SunCollect automated pneumatic sprayer (SunChrom supplied by KR Analytical, Ltd) at a flow rate of 20 μL/min at a linear velocity of 900 mm/min with a 2-mm line distance and Z position of 30 mm in a series of 18 layers. The resulting density of the deuterated standard were 1 ng/mm^2 for [^{2}H$_7$]24R/S-HC; 0.2 ng/mm^2 for each of [^{2}H$_7$]22S-HC, [^{2}H$_7$]22S-HCO, and [^{2}H$_7$]22R-HCO; 4 ng/mm^2 for [^{2}H$_7$]cholesterol; and 1 ng/mm^2 for [^{2}H$_6$]desmosterol (*SI Appendix, Materials and Methods*). The sprayer was thoroughly flushed with about 2 mL of methanol after which cholesterol oxidase (0.264 units/mL in 50 mM KH$_2$PO$_4$, pH7) was sprayed for 18 layers. The first layer was applied at 10 μL/min, the second at 15 μL/min, and then all of the subsequent layers at 20 μL/min to give an enzyme density of 0.05 m units/mm^2. Thereafter, the enzyme-coated slide was placed on a flat dry bed above 30 mL of warm water (37 °C) in a closed pipette-tip box (11.9 cm × 8.2 cm × 8.5 cm) and then incubated at 37 °C for 1 h, after which, the slide was removed and dried in a vacuum desiccator for 15 min. [^{2}H$_5$]GP (6.3 mg/mL bromide salt, in 70% methanol with 5% acetic acid) was sprayed on the dried slide with the same spray parameters as used for spraying cholesterol oxidase. The resulting GP density was 1.21 μg/mm^2. The slide was then placed on a flat dry bed above 30 mL of prewarmed (37 °C) 50% methanol, 5% acetic acid in a covered glass chamber (12 cm × 12 cm × 7.2 cm) and incubated in a water bath at 37 °C for 1 h. The slide was removed and dried in a vacuum desiccator until LC-MS analysis. To analyze sterols containing a naturally occurring oxo group, the cholesterol oxidase spray step was omitted and [^{2}H$_0$]GP (5 mg/mL chloride salt, in 70% methanol with 5% acetic acid) was used as the derivatization agent.

Further details of tissue handling and of MALDI-MSI experiments can be found in *SI Appendix, Materials and Methods*.

Robotic μLESA. Derivatized oxysterols present in 10-μm thick slices of brain tissue were sampled using a TriVersa Nanomate (Advion) with a modified capillary extraction probe (LESA^{PLUS}). The Advion ChipsoftX software was used to capture an optical image of the prepared slide on a flatbed scanner prior to analysis. The same software was also used to define extraction points on the tissue prior to analysis. A 330-μm i.d./794-μm o.d. FEP sleeve was attached to a 200-μm i.d./360-μm o.d. fused silica capillary held in the mandrel of the Advion TriVersa Nanomate; this created a seal when in contact with tissue, preventing the dispersion of sampling extraction solvent (50% methanol) and limiting the sampling area to the internal diameter of the FEP sleeve (*SI Appendix*, Fig. S3 *A* and *B*).

Three microliters of extraction solvent was aspirated into the capillary from the solvent reservoir (R1–R2 in *SI Appendix*, Fig. S4), the mandrel moved robotically to an exact tissue location, and 1 μL of solvent "dispensed" on-tissue and held for 30 s before being aspirated back into the capillary. The mandrel moved once again, and the extract was dispensed into a well of a 384-well plate. The process was repeated twice more with extract dispensed into the same well, before the combined extract was injected via the extraction probe into the sample loop of the LC system (see below). The entire procedure was then repeated on a new extraction point. Multiple points were analyzed to localize oxysterols across brain tissue.

LC-MS(MS^n) at Conventional Flow Rate. LC separations were performed on an Ultimate 3000 UHPLC system (Dionex, now Thermo Scientific). The μLESA extract was delivered from the sample loop onto a trap column (Hypersil Gold C$_{18}$ guard column, 3-μm particle size, 10 × 2.1 mm, Thermo Fisher Scientific) using a loading solvent of 20% methanol at a flow rate of 50 μL/min. The eluent from the trap column containing unreacted GP reagent was delivered to waste (*SI Appendix*, Fig. S4A). After 10 min, the trap column was switched in-line with the analytical column (Hypersil Gold C$_{18}$ column, 1.9-μm particle size, 50 × 2.1 mm, Thermo Fisher). At 11 min, 1 min after valve switching, a gradient was delivered by the binary micropump-2 at 200 μL/min. Mobile phase A consisted of 33.3% methanol, 16.7% acetonitrile, and 0.1% formic acid, and mobile phase B consisted of 63.3% methanol, 31.7% acetonitrile, and 0.1% formic acid. The proportion of B was initially 20% and was raised to 80% B over the next 7 min and maintained at 80% B for 4 min, before being reduced to 20% B in 0.1 min, just after the trap column switched off-line, and the analytical column was reequilibrated for 3.9 min. After switching off-line, at 22 min, the trap column was independently washed with 10 μL of propan-2-ol injected from the Nanomate and delivered with mobile phase B at 200 μL/min for 6 min using micropump-1. At 26 min, the proportion of B washing the analytical column was raised from 20 to 80% over 3 min and held at 80% for a further 5 min before dropping back down to 20% in 0.1 min and equilibrated for 4.9 min, ready for the next surface extraction, giving a total run time of 39 min. At 29 min the trap column was switched back in line with the analytical column and then out of line at 34 min to check for the presence of any sterols retained by the trap column. The gradients are illustrated in *SI Appendix*, Fig. S3 *C* and *D*.

For ESI-MS analysis the column eluent was directly infused into an Orbitrap Elite mass spectrometer (Thermo Scientific) using a H-ESI II probe. To avoid cross-contamination between samples, a blank injection of 6 μL of 50% MeOH was performed with the same 39-min method between injections of tissue extracts.

For each injection, five scan events were performed: one high-resolution scan (120,000 full width at half maximum height definition at *m/z* 400) in the Orbitrap analyzer in parallel to four MS^3 scan events in the linear ion trap. Quantification was by isotope dilution using isotope-labeled standard spayed on-tissue. MS^3 scans were for the transitions [M]$^+$ → [M-Py]$^+$→, where Py is the pyridine group of the GP derivative. For details of nano-LC-MS(MS^n) see *SI Appendix, Materials and Methods*.

Quantification. To achieve reliable quantitative measurements, known amounts of isotope-labeled internal standards [^{2}H$_7$]24R/S-HC, [^{2}H$_6$]desmosterol, [^{2}H$_7$]cholesterol, and [^{2}H$_7$]22S-HCO were sprayed on-tissue prior to the EADSA process. This procedure corrects for variation in derivatization efficiency, surface extraction, extraction area, injection volume, and MS response. Quantification was made from [M]$^+$ ion signals in appropriate reconstructed ion chromatograms (RICs). Approximate quantification of 20S-HC was performed by utilizing the MRM [M]$^+$ → [M-Py]$^+$ → 327.2 transition and quantifying against the transition [M]$^+$ → [M-Py]$^+$ → 353.3 for [^{2}H$_7$]24R/S-HC (*SI Appendix*, Fig. S9F).

Statistics. For three WT mice, and separately for the three knockout mice, unreplicated two-way ANOVA was performed with sterol areal density as dependent variable and mouse and brain region as factors. The interaction between mouse and brain region was used as error variance. The residuals representing the interaction deviations were approximately normally distributed. Tukey's multiple comparisons test was used to identify significant differences between brain regions. Hierarchical cluster analysis using between-groups linkage was used to represent differences and similarities of average sterol areal densities between brain regions averaged across the three biological replicates for each type of mouse, and with the differences represented as squared Euclidean distances. The analyses were performed using IBM SPSS Statistics 22 (IBM Corp) and GraphPad Prism 7.02 software (GraphPad Software Inc). *$P < 0.05$, **$P < 0.01$, ***$P < 0.001$. Whiskers on bar graphs represent 1 SD.

1. J. M. Dietschy, S. D. Turley, Thematic review series: Brain lipids. Cholesterol metabolism in the central nervous system during early development and in the mature animal. *J. Lipid Res.* **45**, 1375–1397 (2004).
2. S. Kanungo, N. Soares, M. He, R. D. Steiner, Sterol metabolism disorders and neurodevelopment-an update. *Dev. Disabil. Res. Rev.* **17**, 197–210 (2013).
3. T. J. Kotti, D. M. Ramirez, B. E. Pfeiffer, K. M. Huber, D. W. Russell, Brain cholesterol turnover required for geranylgeraniol production and learning in mice. *Proc. Natl. Acad. Sci. U.S.A.* **103**, 3869–3874 (2006).
4. D. W. Russell, R. W. Halford, D. M. Ramirez, R. Shah, T. Kotti, Cholesterol 24-hydroxylase: An enzyme of cholesterol turnover in the brain. *Annu. Rev. Biochem.* **78**, 1017–1040 (2009).
5. G. J. Schroepfer, Jr, Oxysterols: Modulators of cholesterol metabolism and other processes. *Physiol. Rev.* **80**, 361–554 (2000).
6. E. G. Lund, J. M. Guileyardo, D. W. Russell, cDNA cloning of cholesterol 24-hydroxylase, a mediator of cholesterol homeostasis in the brain. *Proc. Natl. Acad. Sci. U.S.A.* **96**, 7238–7243 (1999).
7. I. Björkhem, Crossing the barrier: Oxysterols as cholesterol transporters and metabolic modulators in the brain. *J. Intern. Med.* **260**, 493–508 (2006).
8. J. M. Lehmann *et al.*, Activation of the nuclear receptor LXR by oxysterols defines a new hormone response pathway. *J. Biol. Chem.* **272**, 3137–3140 (1997).
9. L. Wang *et al.*, Liver X receptors in the central nervous system: From lipid homeostasis to neuronal degeneration. *Proc. Natl. Acad. Sci. U.S.A.* **99**, 13878–13883 (2002).
10. S. M. Paul *et al.*, The major brain cholesterol metabolite 24(S)-hydroxycholesterol is a potent allosteric modulator of N-methyl-D-aspartate receptors. *J. Neurosci.* **33**, 17290–17300 (2013).
11. A. Radhakrishnan, Y. Ikeda, H. J. Kwon, M. S. Brown, J. L. Goldstein, Sterol-regulated transport of SREBPs from endoplasmic reticulum to Golgi: Oxysterols block transport by binding to Insig. *Proc. Natl. Acad. Sci. U.S.A.* **104**, 6511–6518 (2007).
12. M. Heverin *et al.*, Changes in the levels of cerebral and extracerebral sterols in the brain of patients with Alzheimer's disease. *J. Lipid Res.* **45**, 186–193 (2004).
13. N. Mast *et al.*, Cytochrome P450 27A1 deficiency and regional differences in brain sterol metabolism cause preferential cholestanol accumulation in the cerebellum. *J. Biol. Chem.* **292**, 4913–4924 (2017).
14. J. A. Nelson, S. R. Steckbeck, T. A. Spencer, Biosynthesis of 24,25-epoxycholesterol from squalene 2,3;22,23-dioxide. *J. Biol. Chem.* **256**, 1067–1068 (1981).
15. Y. Wang *et al.*, 24S,25-Epoxycholesterol in mouse and rat brain. *Biochem. Biophys. Res. Commun.* **449**, 229–234 (2014).
16. S. Goyal, Y. Xiao, N. A. Porter, L. Xu, F. P. Guengerich, Oxidation of 7-dehydrocholesterol and desmosterol by human cytochrome P450 46A1. *J. Lipid Res.* **55**, 1933–1943 (2014).
17. D. R. Raleigh *et al.*, Cilia-associated oxysterols activate smoothened. *Mol. Cell* **72**, 316–327.e5 (2018).
18. X. Qi *et al.*, Cryo-EM structure of oxysterol-bound human Smoothened coupled to a heterotrimeric G$_i$. *Nature* **571**, 279–283 (2019).
19. S. Theofilopoulos *et al.*, Brain endogenous liver X receptor ligands selectively promote midbrain neurogenesis. *Nat. Chem. Biol.* **9**, 126–133 (2013).
20. S. Theofilopoulos *et al.*, 24(S),25-Epoxycholesterol and *cholesterol 24S-hydroxylase* (*CYP46A1*) overexpression promote midbrain dopaminergic neurogenesis *in vivo*. *J. Biol. Chem.* **294**, 4169–4176 (2019).
21. S. Theofilopoulos *et al.*, Cholestenoic acids regulate motor neuron survival via liver X receptors. *J. Clin. Invest.* **124**, 4829–4842 (2014).
22. A. Saeed *et al.*, 7α-hydroxy-3-oxo-4-cholestenoic acid in cerebrospinal fluid reflects the integrity of the blood-brain barrier. *J. Lipid Res.* **55**, 313–318 (2014).
23. M. Heverin *et al.*, Crossing the barrier: Net flux of 27-hydroxycholesterol into the human brain. *J. Lipid Res.* **46**, 1047–1052 (2005).
24. S. Meaney *et al.*, Novel route for elimination of brain oxysterols across the blood-brain barrier: Conversion into 7alpha-hydroxy-3-oxo-4-cholestenoic acid. *J. Lipid Res.* **48**, 944–951 (2007).
25. W. J. Griffiths *et al.*, Additional pathways of sterol metabolism: Evidence from analysis of Cyp27a1-/- mouse brain and plasma. *Biochim. Biophys. Acta Mol. Cell Biol. Lipids* **1864**, 191–211 (2019).
26. K. A. Berry *et al.*, MALDI imaging of lipid biochemistry in tissues by mass spectrometry. *Chem. Rev.* **111**, 6491–6512 (2011).
27. M. M. Gessel, J. L. Norris, R. M. Caprioli, MALDI imaging mass spectrometry: Spatial molecular analysis to enable a new age of discovery. *J. Proteomics* **107**, 71–82 (2014).
28. J. L. Norris, R. M. Caprioli, Analysis of tissue specimens by matrix-assisted laser desorption/ionization imaging mass spectrometry in biological and clinical research. *Chem. Rev.* **113**, 2309–2342 (2013).
29. B. Spengler, Mass spectrometry imaging of biomolecular information. *Anal. Chem.* **87**, 64–82 (2015).
30. P. J. Trim *et al.*, Matrix-assisted laser desorption/ionisation mass spectrometry imaging of lipids in rat brain tissue with integrated unsupervised and supervised multivariant statistical analysis. *Rapid Commun. Mass Spectrom.* **22**, 1503–1509 (2008).
31. J. A. Hankin *et al.*, MALDI mass spectrometric imaging of lipids in rat brain injury models. *J. Am. Soc. Mass Spectrom.* **22**, 1014–1021 (2011).

BIOCHEMISTRY

32. K. A. Zemski Berry, W. C. Gordon, R. C. Murphy, N. G. Bazan, Spatial organization of lipids in the human retina and optic nerve by MALDI imaging mass spectrometry. *J. Lipid Res.* **55**, 504–515 (2014).

33. G. J. Patti et al., Nanostructure-initiator mass spectrometry (NIMS) imaging of brain cholesterol metabolites in Smith-Lemli-Opitz syndrome. *Neuroscience* **170**, 858–864 (2010).

34. L. Xu et al., Profiling and imaging ion mobility-mass spectrometry analysis of cholesterol and 7-dehydrocholesterol in cells via sputtered silver MALDI. *J. Am. Soc. Mass Spectrom.* **26**, 924–933 (2015).

35. L. Muller et al., Laser desorption/ionization mass spectrometric imaging of endogenous lipids from rat brain tissue implanted with silver nanoparticles. *J. Am. Soc. Mass Spectrom.* **28**, 1716–1728 (2017).

36. D. F. Cobice et al., Mass spectrometry imaging for dissecting steroid intracrinology within target tissues. *Anal. Chem.* **85**, 11576–11584 (2013).

37. D. F. Cobice et al., Spatial localization and quantitation of androgens in mouse testis by mass spectrometry imaging. *Anal. Chem.* **88**, 10362–10367 (2016).

38. D. F. Cobice et al., Quantification of 11β-hydroxysteroid dehydrogenase 1 kinetics and pharmacodynamic effects of inhibitors in brain using mass spectrometry imaging and stable-isotope tracers in mice. *Biochem. Pharmacol.* **148**, 88–99 (2018).

39. B. Flinders, J. Morrell, P. S. Marshall, L. E. Ranshaw, M. R. Clench, The use of hydrazine-based derivatization reagents for improved sensitivity and detection of carbonyl containing compounds using MALDI-MSI. *Anal. Bioanal. Chem.* **407**, 2085–2094 (2015).

40. F. P. Barré et al., Derivatization strategies for the detection of triamcinolone acetonide in cartilage by using matrix-assisted laser desorption/ionization mass spectrometry imaging. *Anal. Chem.* **88**, 12051–12059 (2016).

41. S. Shimma et al., Microscopic visualization of testosterone in mouse testis by use of imaging mass spectrometry. *Anal. Bioanal. Chem.* **408**, 7607–7615 (2016).

42. A. K. Badu-Tawiah, D. I. Campbell, R. G. Cooks, Reactions of microsolvated organic compounds at ambient surfaces: Droplet velocity, charge state, and solvent effects. *J. Am. Soc. Mass Spectrom.* **23**, 1077–1084 (2012).

43. K. Karu et al., Liquid chromatography-mass spectrometry utilizing multi-stage fragmentation for the identification of oxysterols. *J. Lipid Res.* **48**, 976–987 (2007).

44. H. Roberg-Larsen et al., Highly automated nano-LC/MS-based approach for thousand cell-scale quantification of side chain-hydroxylated oxysterols. *J. Lipid Res.* **55**, 1531–1536 (2014).

45. P. J. Crick et al., Quantitative charge-tags for sterol and oxysterol analysis. *Clin. Chem.* **61**, 400–411 (2015).

46. G. J. Van Berkel, V. Kertesz, K. A. Koeplinger, M. Vavrek, A. N. Kong, Liquid microjunction surface sampling probe electrospray mass spectrometry for detection of drugs and metabolites in thin tissue sections. *J. Mass Spectrom.* **43**, 500–508 (2008).

47. W. B. Parson et al., Analysis of chloroquine and metabolites directly from whole-body animal tissue sections by liquid extraction surface analysis (LESA) and tandem mass spectrometry. *J. Mass Spectrom.* **47**, 1420–1428 (2012).

48. L. Lamont et al., Integration of ion mobility MS^E after fully automated, online, high-resolution liquid extraction surface analysis micro-liquid chromatography. *Anal. Chem.* **89**, 11143–11150 (2017).

49. D. J. Ryan et al., Protein identification in imaging mass spectrometry through spatially targeted liquid micro-extractions. *Rapid Commun. Mass Spectrom.* **32**, 442–450 (2018).

50. R. Almeida, J. K. Pauling, E. Sokol, H. K. Hannibal-Bach, C. S. Ejsing, Comprehensive lipidome analysis by shotgun lipidomics on a hybrid quadrupole-orbitrap-linear ion trap mass spectrometer. *J. Am. Soc. Mass Spectrom.* **26**, 133–148 (2015).

51. M. Ogundare et al., Cerebrospinal fluid steroidomics: Are bioactive bile acids present in brain? *J. Biol. Chem.* **285**, 4666–4679 (2010).

52. A. Meljon, Y. Wang, W. J. Griffiths, Oxysterols in the brain of the cholesterol 24-hydroxylase knockout mouse. *Biochem. Biophys. Res. Commun.* **446**, 768–774 (2014).

53. N. Mast, J. B. Lin, K. W. Anderson, I. Bjorkhem, I. A. Pikuleva, Transcriptional and post-translational changes in the brain of mice deficient in cholesterol removal mediated by cytochrome P450 46A1 (CYP46A1). *PLoS One* **12**, e0187168 (2017).

54. Y. K. Paik, J. T. Billheimer, R. L. Magolda, J. L. Gaylor, Microsomal enzymes of cholesterol biosynthesis from lanosterol. Solubilization and purification of steroid 8-isomerase. *J. Biol. Chem.* **261**, 6470–6477 (1986).

55. E. S. Lein et al., Genome-wide atlas of gene expression in the adult mouse brain. *Nature* **445**, 168–176 (2007).

56. L. Iuliano, Cholesterol metabolites exported from human brain. *Steroids* **99**, 189–193 (2015).

57. R. Shinkyo et al., Conversion of 7-dehydrocholesterol to 7-ketocholesterol is catalyzed by human cytochrome P450 7A1 and occurs by direct oxidation without an epoxide intermediate. *J. Biol. Chem.* **286**, 33021–33028 (2011).

58. R. C. Murphy, K. M. Johnson, Cholesterol, reactive oxygen species, and the formation of biologically active mediators. *J. Biol. Chem.* **283**, 15521–15525 (2008).

59. E. G. Lund et al., Knockout of the cholesterol 24-hydroxylase gene in mice reveals a brain-specific mechanism of cholesterol turnover. *J. Biol. Chem.* **278**, 22980–22988 (2003).

60. H. Roberg-Larsen, M. F. Strand, S. Krauss, S. R. Wilson, Metabolites in vertebrate Hedgehog signaling. *Biochem. Biophys. Res. Commun.* **446**, 669–674 (2014).

61. Y. Y. Lin, M. Welch, S. Lieberman, The detection of 20S-hydroxycholesterol in extracts of rat brains and human placenta by a gas chromatograph/mass spectrometry technique. *J. Steroid Biochem. Mol. Biol.* **85**, 57–61 (2003).

62. L. Puglielli et al., Alzheimer disease beta-amyloid activity mimics cholesterol oxidase. *J. Clin. Invest.* **115**, 2556–2563 (2005).

63. I. Björkhem, Five decades with oxysterols. *Biochimie* **95**, 448–454 (2013).

64. K. Schümann, B. Szegner, B. Kohler, M. W. Pfaffl, T. Ettle, A method to assess 59Fe in residual tissue blood content in mice and its use to correct 59Fe-distribution kinetics accordingly. *Toxicology* **241**, 19–32 (2007).

65. Y. F. Chiang et al., Differential regulation of the human CYP11A1 promoter in mouse brain and adrenals. *J. Cell. Physiol.* **226**, 1998–2005 (2011).

66. J. R. Dwyer et al., Oxysterols are novel activators of the hedgehog signaling pathway in pluripotent mesenchymal cells. *J. Biol. Chem.* **282**, 8959–8968 (2007).

67. S. Nachtergaele et al., Oxysterols are allosteric activators of the oncoprotein Smoothened. *Nat. Chem. Biol.* **8**, 211–220 (2012).

68. D. Nedelcu, J. Liu, Y. Xu, C. Jao, A. Salic, Oxysterol binding to the extracellular domain of Smoothened in Hedgehog signaling. *Nat. Chem. Biol.* **9**, 557–564 (2013).

69. A. Saadane, N. Mast, T. Dao, B. Ahmad, I. A. Pikuleva, Retinal hypercholesterolemia triggers cholesterol accumulation and esterification in photoreceptor cells. *J. Biol. Chem.* **291**, 20427–20439 (2016).

70. O. Knittelfelder et al., Shotgun lipidomics combined with laser capture microdissection: A tool to analyze histological zones in cryosections of tissues. *Anal. Chem.* **90**, 9868–9878 (2018).

71. S. M. Cologna, Mass spectrometry imaging of cholesterol. *Adv. Exp. Med. Biol.* **1115**, 155–166 (2019).

72. J. Soltwisch et al., Mass spectrometry imaging with laser-induced postionization. *Science* **348**, 211–215 (2015).

73. T. B. Angerer, M. Dowlatshahi Pour, P. Malmberg, J. S. Fletcher, Improved molecular imaging in rodent brain with time-of-flight-secondary ion mass spectrometry using gas cluster ion beams and reactive vapor exposure. *Anal. Chem.* **87**, 4305–4313 (2015).

74. N. J. Starr et al., Age-related changes to human stratum corneum lipids detected using time-of-flight secondary ion mass spectrometry following in vivo sampling. *Anal. Chem.* **88**, 4400–4408 (2016).

75. P. Sjövall et al., Imaging the distribution of skin lipids and topically applied compounds in human skin using mass spectrometry. *Sci. Rep.* **8**, 16683 (2018).

76. J. F. Frisz et al., Sphingolipid domains in the plasma membranes of fibroblasts are not enriched with cholesterol. *J. Biol. Chem.* **288**, 16855–16861 (2013).

77. L. Boussicault et al., CYP46A1, the rate-limiting enzyme for cholesterol degradation, is neuroprotective in Huntington's disease. *Brain* **139**, 953–970 (2016).